Thesis for The Degree of Licentiate of Engineering

Measuring atmospheric ice mass with the Arctic Weather Satellite

Peter McEvoy

Department of Environmental and Energy Sciences
Chalmers University of Technology
Gothenburg, Sweden, 2026

Measuring atmospheric ice mass with the Arctic Weather Satellite

Peter McEvoy

Division of Geoscience and Remote Sensing
Department of Environmental and Energy Sciences
Chalmers University of Technology
SE-412 96 Göteborg,
Sweden
Phone: +46(0)31 772 1000

Cover: Ice property estimates derived from real microwave and sub-millimetre measurments from the Arctic Weather Satellite's radiometer. The properties estimated are: frozen water path ($\mathrm{kg\,m^{-2}}$), the mass of ice in the vertical column through the atmosphere; Z_m (km), the mass-weighted mean altitude of ice within the column; D_m (µm), the mass-weighted mean ice particle size within the column.

Printed by Chalmers Digitaltryck,
Gothenburg, Sweden 2026.

Measuring atmospheric ice mass with the Arctic Weather Satellite

Peter McEvoy

Department of Environmental and Energy Sciences
Chalmers University of Technology

Abstract

Atmospheric ice, consisting of various sizes of ice particles in clouds or precipitation, plays critical roles in weather and climate processes. Yet, large uncertainties remain in atmospheric ice estimates and the understanding of cloud formation processes, limiting our ability to predict severe weather and the effects of a changing climate.

Satellites carrying specialized cloud profiling radars provide the most accurate global measurements. However, their coverage is limited to a swath of roughly 1 km. Passive instruments provide much larger spatial coverage, yet, for these, a gap in sensitivity to ice particles exists in the sub-millimetre region (frequencies above 300 GHz) between microwave and infrared wavelengths. Simulations in the 1990s and 2000s established the potential of sub-millimetre observations, demonstrating that such measurements are sensitive to ice particles that account for a significant fraction of atmospheric ice mass.

In 2024, the Arctic Weather Satellite (AWS) was launched with novel 325 GHz channels, making it the first satellite to provide regular earth-facing measurements of the sub-millimetre band. In 2029, the EPS-Sterna programme is set to launch a constellation of six AWS-like satellites. Another space-borne instrument, the Ice Cloud Imager, is due to launch in 2026, with channels at 183, 325, 448, and 664 GHz. Together, these missions will provide a wealth of long-term sub-millimetre data with high spatial and temporal coverage.

This thesis asses the utility of these measurements from AWS and develops ice property estimates from them. Radiative transfer simulations of AWS observations match statistical distributions from real observations over ocean surfaces, confirming that current simulators already show ability in handling the new sub-millimetre channels, essential for operational utilization of these channels in weather centres and for accurate ice property retrievals.

The main contribution is the development of sub-millimetre-informed ice property estimates from AWS. The retrieval method estimates frozen water path, and associated mass-weighted mean altitude and particle size. Statistical comparisons with radar/lidar-based datasets show matching local and zonal means. This has resulted in a public data product of sub-millimetre-based ice mass property estimates, the first of its kind.

Keywords: remote sensing, sub-millimetre, atmospheric ice, retrievals

List of Publications

Appended publications

This thesis is based on the following publications:

Paper 1: **P. McEvoy**, E. May, P. Eriksson, *The Arctic Weather Satellite, introducing a new wavelength range for ice hydrometeor retrievals*
Submitted to Atmospheric Measurement Techniques.

Paper 2: D. I. Duncan, N. Bormann, M. D. Fielding, A. J. Geer, **P. McEvoy**, E. May, P. Eriksson, *A first global view of sub-millimetre radiances from the Arctic Weather Satellite*
Earth and Space Science, in review.

Other publications

1. P. Eriksson, A. Emrich, K. Kempe, J. Riesbeck, A. Aljarosha, O. Auriacombe, J. Kugelberg, E. Hekma, R. Albers, A. Murk, S. M. Pedersen, L. John, J. Stake, **P. McEvoy**, B. Rydberg, A. Dybbroe, A. Thoss, A. Canestri, C. Accadia, P. Colucci, D. Gherardi, V. Kangas, *The Arctic Weather Satellite radiometer*
Atmospheric Measurement Techniques, 18, 4709–4729, https://doi.org/10.5194/amt-18-4709-2025, 2025.

Acknowledgment

Thank you to my supervisor, Patrick Eriksson, for always making time for discussions and my questions, clear guidance, and the effort put into ensuring that our education and work lives up to a good standard. I am very grateful for the opportunity to work with satellite remote sensing and deeply appreciate his guidance in introducing me to this field.

I also want to thank the informal group of colleagues around our subject area of remote sensing of clouds. The group makes me feel welcome, and I am grateful for the opportunities that arise when we can collaborate on projects. In particular, Eleanor May and Adrià Amell, whose help with projects and research insight has meant a great deal.

Heartfelt thanks to Jonna and my family: Aina, Conni, and Fintan.

The work presented in this thesis is supported by the Swedish National Space Agency grant 2023-00139.

Contents

Abstract **i**

List of Publications **iii**

Acknowledgment **v**

I Summary **1**

1 Introduction **3**
1.1 Atmospheric ice and its importance 3
1.2 Radiative transfer of microwave radiation 5
1.2.1 Quantities 5
1.2.2 The radiative transfer equation 7
1.2.3 Ice hydrometeors and bulk properties 9
1.2.4 Ice hydrometeor impact on the extinction coefficient . . 11
1.3 Remote sensing of clouds 12
1.3.1 Sensor types and ice property retrievals 13
1.3.2 The Arctic Weather Satellite 15
1.3.3 The Ice Cloud Imager 18
1.4 Research context 18

2 Summary of appended papers **21**
2.1 Paper 1 21
2.2 Paper 2 22

Bibliography **23**

II Appended Papers **27**

Part I

Summary

Chapter 1

Introduction

This chapter introduces the main focus of this thesis: measuring and quantifying atmospheric ice mass, along with the theoretical and historical background to the research presented.

The chapter begins by explaining why such measurements matter, introduces the relevant quantities and relationships from radiative transfer theory, lists the main approaches and instruments used to detect atmospheric ice, and concludes by reviewing the prior research on which this work builds.

1.1 Atmospheric ice and its importance

Atmospheric ice, including ice particles within clouds and precipitation such as snow or hail, plays several important roles in weather and climate. It drives storm development, serves, alongside water vapour and liquid, as a primary mechanism for short-term water transport across the globe, and influences Earth's energy balance.

Yet, the processes governing cloud formation and the atmospheric ice content remains poorly understood. Moreover, how clouds and ice will respond to a changing climate is even more uncertain.

It has been stated with high confidence that clouds remain the largest contribution to overall uncertainty in climate feedbacks (Intergovernmental Panel on Climate Change (IPCC) 2023, p. 94). To aid in tracking Earth's changing climate, the concept of *essential climate variables* (ECVs; Bojinski et al. 2014) was developed to emphasize key indicators. The set of ECVs have since been compiled (World Meteorological Organization 2016). Among these, *cloud ice water path*, here defined as the amount of ice through a column of the atmosphere.

The following sections outline the role atmospheric ice plays in weather, the hydrological cycle and Earth's energy balance.

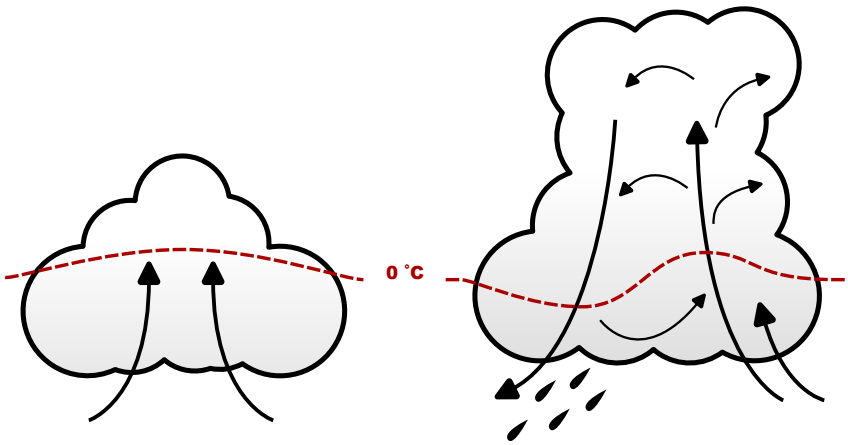

Figure 1.1: Illustration of a cumulus cloud and a developed convective cell. Arrows indicate updrafts, downdrafts and air deviating from them. The convective cell has precipitation at the cloud bottom, indicated by raindrops.

Weather

The formation and melting of ice plays a driving role in precipitation and the development of storms. Globally, 50% of all events with more than 1 mm precipitation per day is attributed to ice formation in clouds (Field and Heymsfield 2015).

Clouds form when warm moist air rises into cooler, drier air, causing condensation of moisture into water droplets, as illustrated in Figure 1.1. When the cloud extends into regions with surrounding freezing air, water vapour and water droplets freeze. This phase change from gas or liquid to solid releases *latent heat* into the surrounding environment. This added heat further intensifies the updraft, driving further cloud growth with a chance of forming a convective cell. The convective cell sustains itself by repeatedly reinforcing the draft pulling in new moist warm air from its surrounding.

Frozen particles within this system will start to descend, with some leaving the cell while others are captured again by the updraft, creating a process where ice particles grow by repeatedly colliding with new moisture and other ice particles (Lohmann et al. 2016, Chapter 8).

Processes like these are responsible for heavy rainfall, hailstorms, snowfall and thunderstorms. Understanding and observing them is important for weather forecasting, disaster preparedness and early warning of flooding and other extreme weather events.

Hydrological cycle

The *hydrosphere* comprises all water on Earth, distributed across multiple reservoirs. Most water resides in the Earth's mantle, oceans, and ice sheets,

where it remains for long timescales. The atmosphere holds only a small fraction of this water, yet it is responsible for the largest rate of exchange, with a mean residency time of roughly 10 days (Wallace and Hobbs 2006, Chapter 2.2).

This atmospheric exchange occurs through evaporation and precipitation. Evaporation is a primary mechanism for transporting water and heat from Earth's surface to the atmosphere. By precipitation as rain or snow, water is returned to Earth's surface. Globally, evaporation must equal precipitation to maintain equilibrium. Locally, however, precipitation varies geographically and atmospheric water is transported unevenly across regions. As the climate changes, understanding and tracking how these exchange dynamics shift determines our capacity to predict agricultural impacts, floods, and droughts.

Energy balance

Clouds impact Earth's energy balance in two opposite ways. First, they reflect solar radiation that would otherwise be absorbed by Earth, back out to space, producing a *negative radiative forcing* (a cooling effect). Second, they trap thermal radiation from Earth whilst having varying degrees of transparency to incoming solar radiation, producing a *positive radiative forcing* (a warming effect). Globally, clouds cause a net negative radiative forcing. This negative effect is roughly six times larger than the positive radiative forcing from doubled carbon dioxide relative to pre-industrial conditions (Lohmann et al. 2016, Chapter 11.4).

However, how cloud-coverage and frequency of different cloud types will develop under a changing climate is uncertain. Yet, there is high confidence that these changes will produce a net *positive climate feedback*, i.e. cloud changes will amplify rather than dampen warming, the magnitude of this feedback, however, is highly uncertain (Intergovernmental Panel on Climate Change (IPCC) 2023, p. 95). Climate model simulations, satellite observations, and explicit cloud simulations have identified several cloud climate feedback mechanisms. These are processes where a changing climate alters cloud characteristics in ways that further increase or decrease the radiative forcing. This is an active area of research where satellite observations are ultimately needed for detecting and verifying such feedback mechanisms.

1.2 Radiative transfer of microwave radiation

This section introduces the basic quantities and the fundamental theoretical framework for describing the radiative effects measured in this work. Ulaby and Long (2014, Chapter 6), and Sharkov (2003, Chapter 9) have been used as references for this section.

1.2.1 Quantities

In remote sensing, the physical state of a medium or object surface is inferred from measured electromagnetic radiation. Radiative transfer is used as a

theoretical framework to model the electromagnetic interactions that result in the radiation being measured.

A key quantity in radiative transfer is the *spectral radiance* I_f expressed as $\mathrm{W\,m^{-2}\,sr^{-1}\,Hz^{-1}}$. It describes the amount of energy propagating in a given direction, per second per projected area per steradians for a given frequency f.

For atmospheric remote sensing, the radiance source can be the instrument itself, solar radiation, or thermal emission from solids, liquids, and gases. In passive observations at thermal infrared wavelengths and beyond, thermal emission dominates.

The thermally emitted radiance depends on temperature, molecular composition and surface properties, such as roughness for solid objects and liquids. The viewing direction and observation wavelength also influence the measured radiance.

The *black body radiator* is a helpful idealised object that absorbs all incoming radiation and emits only thermal radiation according to its temperature. This object can be used as a starting point to model emissive objects and media. Planck's law gives an expression for the spectral radiance emitted by a black-body B_f at frequency f with temperature T:

$$B_f(T) = \frac{2hf^3}{c^2}\left(\frac{1}{e^{hf/kT}-1}\right), \tag{1.1}$$

where h is Planck's constant, c is the speed of light in vacuum and k is Boltzmann's constant.

In microwave and infrared remote sensing, Planck's law is also used to express the *brightness temperature* T_b as a convenient measure of radiance: the temperature a black body radiator would need to be at to achieve the observed spectral radiance,

$$T_b = \frac{hf}{k}\ln^{-1}\left(1+\frac{2hf^3}{I_f c^2}\right). \tag{1.2}$$

As indicated, the black body radiator is an idealization and fails to model phenomenon such as emission lines from molecular energy state transitions and polarization. Such effects are represented in the medium's *emissivity* e_f, defined by the ratio between the black body radiance and the emitted radiance,

$$e_f = \frac{I_f}{B_f(T)}. \tag{1.3}$$

This factor is dependent on variables such as medium properties, surface roughness, viewing direction, sensor polarization state and frequency.

Objects and media also absorb radiation. This is represented by the *absorptivity* a_f and is defined by the ratio between the absorbed and incident radiance:

$$a_f = \frac{I_{f,\mathrm{absorbed}}}{I_{f,\mathrm{incident}}}. \tag{1.4}$$

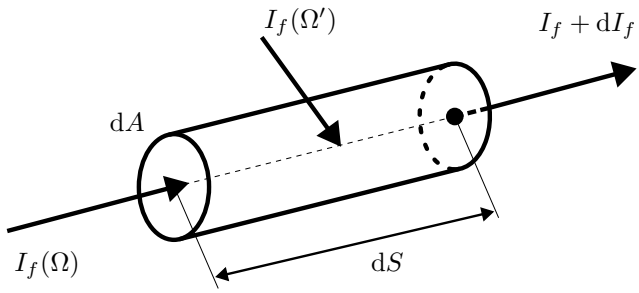

Figure 1.2: Illustration of an infinitesimal cylinder in a medium oriented in the propagation direction Ω with cylinder length $\mathrm{d}S$. Incident radiance $I_f(\Omega)$ along propagation direction Ω enters the cylinder. The outgoing radiance exists at the other end and is the sum of the incoming radiance altered by the cylinder's contribution: $I_f + \mathrm{d}I_f$. Scattering causes some radiance to scatter away and causes radiance from elsewhere $I_f(\Omega')$ to scatter into the propagation path. Radiance scattered away from the propagation path is not shown in the illustration.

Finally, media can also scatter radiation. When radiation enters scattering media, two effects occur: first, radiance may scatter away from the propagation path, reducing the radiance reaching the observer; second, scattered radiation from elsewhere can enter the propagation path, adding to the total radiance. Scattering is a highly directionally-dependent process, unlike absorption and emission in gaseous media.

The key quantities for scattering are the particle's *scattering cross-section* $\sigma_{s,f}$ (m^2), which describes how effective a particle is at causing a scattering event, and the *phase function* $p_f(\Omega' \to \Omega)$, which is the probability distribution of scattering for given incident Ω' and outgoing direction Ω. The phase function is normalized so that $\frac{1}{4\pi}\int_{\Omega=4\pi} p_f(\Omega; \to \Omega)\mathrm{d}\Omega = 1$. Both quantities are dependent on the media's properties and the frequency and polarization state of the observer.

In the following section, these quantities are put together into the radiative transfer equation, modelling how media interacts with radiance.

1.2.2 The radiative transfer equation

There are three main processes when modelling the interaction between electromagnetic radiation and matter: *absorption*, *emission* and *scattering*. Figure 1.2 illustrates an infinitesimal cylinder in a medium through which these radiative transfer processes will be modelled. In a vacuum, radiance stays constant with respect to the propagation distance $\mathrm{d}S$:

$$\frac{\mathrm{d}I_{f,\mathrm{vacuum}}}{\mathrm{d}S} = 0\,.$$

Absorption A homogeneous medium consisting of a single type of object i (a molecular species or a scattering object) has a frequency-dependent absorption cross-section $\sigma_{a,f,i}\,(\mathrm{m}^2)$, quantifying the absorption effectiveness. Multiple object types combine via a weighted sum to form the *absorption coefficient* $\kappa_{a,f} = \sum_i N_i \sigma_{a,f,i}\ (\mathrm{m}^{-1})$, quantifying the attenuation per unit length and represents a *bulk property* of the medium. Here, N_i is the *number density* for each object type, stating the number of particles per unit volume. The incident radiance propagating through our cylinder will be attenuated accordingly:

$$\mathrm{d}I_{f,\text{absorption}} = -\kappa_{a,f} I_f \mathrm{d}S\,. \tag{1.5}$$

Thermal emission The medium will also spontaneously emit thermal radiation due to its temperature. To simplify, we assume *local thermodynamic equilibrium* (LTE), meaning that the medium has molecular collisions frequently enough for the local area to be considered in thermal equilibrium, and that its emission depends solely on temperature. I.e. there are no emission effects due to incident radiation other than indirectly contributing to the medium's temperature. This is true for altitudes below 60 km (Wallace and Hobbs 2006, Chapter 4.3.5). The medium's emission can then be modelled by a black body radiator, modulated by the medium's emissivity: $I_{f,\text{emission}} = e_f B_f(T)$. For a mixture of species, the emission can be added together, producing the *emissivity coefficient* κ_{emission}, analogous to the absorption coefficient $\kappa_{a,f}$. However, under LTE, Kirchoff's law applies and emissivity equals absorptivity, i.e. $e_f = a_f$. Similarly, the emissivity coefficient equals the absorption coefficient, i.e. $\kappa_{\text{emission},f} = \kappa_{a,f}$. The contribution from thermal emission is thus:

$$\mathrm{d}I_{f,\text{thermal emission}} = \kappa_{a,f} B_f(T) \mathrm{d}S\,. \tag{1.6}$$

Scattering Scattering is expressed with the medium's scattering cross-section $\sigma_{s,f}$ and phase function $p_f(\Omega' \to \Omega)$ introduced in Section 1.2.1. The medium will scatter away radiance and reduce the energy in the propagation direction Ω corresponding to $\sigma_{s,f} I_f(\Omega)\mathrm{d}S$. Radiance from elsewhere has a chance of scattering into the propagation path, thereby adding to the radiance. This contribution is modelled by integrating radiance $I_f(\Omega')$ from all other directions Ω' weighted by the particle's phase function, making the added radiance into the original propagation direction Ω equal to $\sigma_{s,f} \frac{1}{4\pi} \int_\Omega I_f(\Omega') p_f(\Omega' \to \Omega)\mathrm{d}\Omega'$.

Similarly to $\kappa_{a,f}$, the scattering coefficient $\kappa_{s,f}$ is the bulk property for multiple different scattering particles. If the particles are *independent scatterers*, i.e. have sufficient spacing in between them with respect to the wavelength to be seen as individual objects, the contributions can be combined additively: $\kappa_{s,f} = \sum_i N_i \sigma_{s,f,i}$ with the phase function combined as $p_f = \frac{1}{\kappa_{s,f}} \sum_i N_i \sigma_{s,f,i} p_{f,i}$.

Together, the total contribution from scattering is,

$$\mathrm{d}I_{f,\text{scattering}} = \underbrace{\left(\kappa_{s,f} \frac{1}{4\pi} \int_{\Omega=4\pi} I_f(\Omega') p_f(\Omega' \to \Omega)\mathrm{d}\Omega'\right)}_{\text{scattered into}} \mathrm{d}S - \underbrace{\kappa_{s,f} I_f(\Omega)}_{\text{scattered away}} \mathrm{d}S\,. \tag{1.7}$$

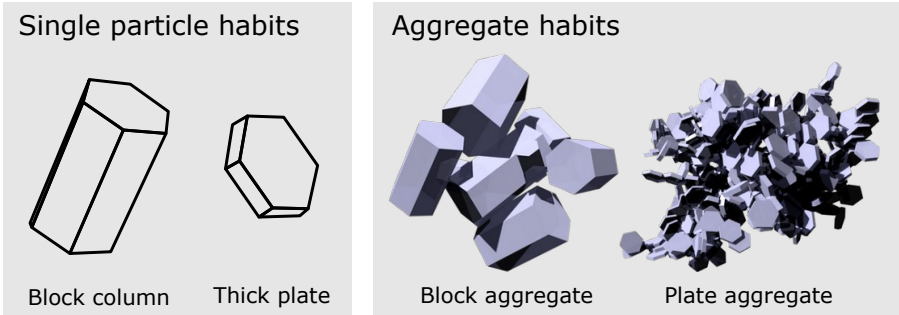

Figure 1.3: Two examples of both single particle habits and aggregate habits. Particle shapes from Eriksson et al. (2018, CC BY 4.0).

The added radiance from scattering is called the scattering source function $J_s = \frac{1}{4\pi}\int_{\Omega=4\pi} I_f(\Omega')p_f(\Omega' \to \Omega)\mathrm{d}\Omega'$. The gained radiance from thermal emission is called the emission source function J_a and under LTE, $J_a = B_f(T)$.

Adding the contributions from absorption, thermal emission, and scattering together, we get,

$$\mathrm{d}I_f = \underbrace{(\kappa_{a,f}J_a + \kappa_{s,f}J_s)}_{\text{sources}}\mathrm{d}S - \underbrace{(\kappa_{a,f}I_f + \kappa_{s,f}I_f)}_{\text{extinction}}\mathrm{d}S \tag{1.8}$$

The terms have been grouped into *sources* (the part that contributes to radiance) and *extinction* (the part that reduces radiance).

The *extinction coefficient* $\kappa_{e,f}$ is the sum of the absorption and scattering coefficient, $\kappa_{e,f} = \kappa_{a,f} + \kappa_{s,f}$. The *single-scattering albedo* is $a = \frac{\kappa_{s,f}}{\kappa_{e,f}}$ and is a measure of the importance of scattering relative to absorption. With these new terms, equation (1.8) can be further reduced:

$$\begin{aligned}\mathrm{d}I_f &= \kappa_{e,f}\underbrace{((1-a)J_a + aJ_s)}_{J}\mathrm{d}S - \kappa_{e,f}I_f\mathrm{d}S \\ &= \kappa_{e,f}(J - I_f)\mathrm{d}S\,.\end{aligned} \tag{1.9}$$

We arrived at this equation by introducing several new terms, including the extinction coefficient. The extinction coefficient $\kappa_{e,f}$ combines absorption and scattering into a single quantity. It is this quantity together with the phase function p_f and emission that is measured and is the signal that carries information about the physical state of the medium.

1.2.3 Ice hydrometeors and bulk properties

The work in this thesis concerns itself with the emission, absorption, and scattering of radiance due to *ice hydrometeors*, an umbrella term for tiny ice crystal particles, larger ice crystal aggregates (snow), and hail.

Depending on environmental factors such as temperature and humidity, ice crystals follow distinct geometrical shapes as they grow, called *habits*. Through collisions, multiple crystals can attach and form growing *aggregates*. See Figure 1.3. Crystal growth and aggregate formation is a dynamical process depending on multiple factors producing a distribution of sizes and habits.

In practice, the particle number concentration for each particle type is described using simplified mathematical models which are fitted to agree with measurements. A *particle size distribution* (PSD) is used to model how numerous particles of different sizes are, given altitude, temperature and other variables. The exponential PSD (Marshall and Palmer 1948) is a commonly used PSD for rain, but also ice:

$$n(d_{\max}) = N_0 \exp\left(-\Lambda d_{\max}\right), \tag{1.10}$$

where the N_0 and Λ are parameters adjusted to fit measurements of ice particle sizes for certain habits. The particle size metric $d_{\max}$ is the maximum diameter of the particle across all possible cross-sectional planes. Because particle shapes and sizes vary widely, a direct expression for the particle's mass is not feasible. Instead, an approximative model is commonly used,

$$m(d_{\max}) = \alpha d_{\max}^{\beta}, \tag{1.11}$$

where α describes the particle growth with size and β describes the particle's porosity.

There are other size metrics that can be used, one being the volume equivalent diameter of the particle, i.e. the diameter of the resulting sphere from packing all of the particle's ice together. Using the expression for mass Eq. (1.11), the two metrics can be related by

$$d_{\mathrm{veq}} = \sqrt[3]{6m/\pi\rho}, \tag{1.12}$$

with m and ρ being the particle mass and density of solid ice, respectively.

One of the main quantities for atmospheric ice is the *frozen water content* (FWC), the mass of ice per unit volume ($\mathrm{kg\,m^{-3}}$),

$$\mathrm{FWC} = \int_0^{\infty} m(d_{\mathrm{veq}}) n(d_{\mathrm{veq}}) \mathrm{d}d_{\mathrm{veq}}, \tag{1.13}$$

where $n(d_{\mathrm{veq}})$ is the PSD, d_{veq} is the diameter, and the particle mass is given by,

$$m(d_{\mathrm{veq}}) = \frac{\pi\rho d_{\mathrm{veq}}^3}{6}. \tag{1.14}$$

Integrating FWC vertically gives the *frozen water path* (FWP),

$$\mathrm{FWP} = \int_{z_0}^{\infty} \mathrm{FWC}\, \mathrm{d}z, \tag{1.15}$$

the mass of ice within the vertical column ($\mathrm{kg\,m^{-2}}$) through the atmosphere. The term FWP is used here instead of cloud ice water path to address the ambiguity of if precipitating ice hydrometeors should be included in cloud ice or not.

Habit shape, aggregate structure, and sizes affect the absorption, scattering and the phase function of ice hydrometeors. In the microwave and sub-millimetre range, ice hydrometeors have high scattering albedo, meaning that the scattering cross-section $\sigma_{s,f}$ and phase function p_f dominate changes in measured radiance.

1.2.4 Ice hydrometeor impact on the extinction coefficient

As mentioned, $\kappa_{a,f}$, $\kappa_{e,f}$ and the phase function p_f affect measured values from electromagnetic sensors. These measurements carry information about the medium under observation, such as the molecules present in the medium (identifiable through transition lines) or the scattering aerosols and hydrometeors.

A scattering particle's impact on the measured radiance is determined by the particle's *single-scattering properties* (SSPs): the extinction cross-section $\sigma_{e,f} = \sigma_{a,f} + \sigma_{s,f}$ and scattering phase function p_f. They depend on the particle shape, size, material, temperature, polarization state and wavelength of the interacting radiation.

Theoretical models such as Mie theory allow these properties to be derived analytically for spherical particles. Ice hydrometeors, however, generally have more complicated shapes. For such particles, electromagnetic interactions against the particle and its geometry are numerically simulated for the different combinations of dependent parameters. This results in a lookup-table of SSP values for that particle type as a function of these variables.

To represent a medium of different particles, the SSPs for each particle type i (habit and size) is multiplied with their corresponding number densities N_i (introduced in Section 1.2.2), describing the number of particles of type i per unit volume. These contributions are summed across all particle types to give the extinction coefficient for the medium,

$$\kappa_{e,f} = \sum_i N_i \sigma_{e,f,i}\,. \tag{1.16}$$

This is a bulk property of the medium representing both scattering and absorption.

Contributions from the phase functions are also combined through summation. Again, in order for these quantities to be combined additively, the particles must be independently scattering, see section 1.2.2.

The particle number concentration can be estimated for a given FWC by assuming a particle habit and PSD (Eq. 1.10), and then using the FWC expression (Eq. 1.13), to adjust Λ to match the observed FWC quantity.

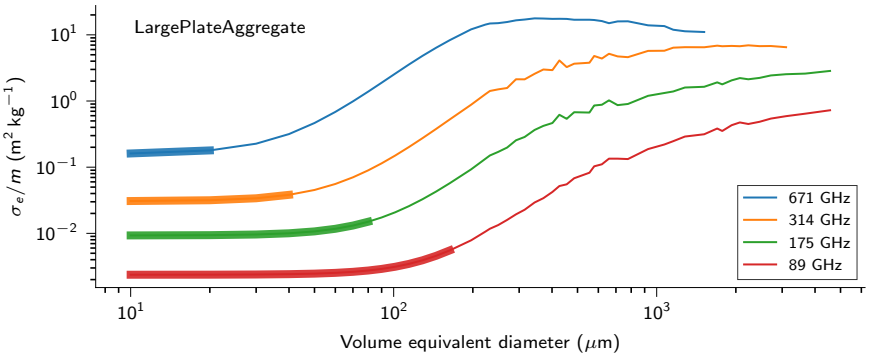

Figure 1.4: Extinction cross-section $\sigma_{e,f}$ normalized by mass for a "plate aggregate" particle over different aggregate sizes for four different frequencies. These values are for temperature 190 K. The approximate region where Rayleigh conditions apply, i.e. where size parameter $x = \pi d_{\max}/\lambda << 1$, is marked by thicker lines.

Figure 1.4 shows the extinction cross-section per unit mass for different sizes of a ice hydrometeor aggregate for four different frequencies. The curves show an offset trend: at smaller sizes, mass-normalised extinctions remains nearly constant in the logarithmic scale, but as size increases, the slope steepens before slowly levelling off. This behaviour reflects two scattering regimes. For smaller particles at these frequencies, Rayleigh conditions apply, where the absorption component of the extinction dominates ($\sigma_a \propto d^3_{\max}/\lambda$ compared to $\sigma_s \propto d^6_{\max}/\lambda^4$). As the particle increases in size, the Rayleigh regime ceases and the resulting extinction behaviour becomes more dependent on frequency and particle shape, making a general expression across these variables difficult to derive.

1.3 Remote sensing of clouds

In section 1.1, we established that observing clouds and the ice within them is important for weather forecasting, tracking climate change, and for providing observations for cloud process research.

Atmospheric ice can be measured in multiple ways. From the ground, weather radars and specialized cloud radars can measure ice in the surrounding atmosphere and profile its vertical distribution. In the air, aeroplanes equipped with special instruments can fly through clouds measuring ice particles. However, only measurements from space can provide regular global estimates of ice mass.

Satellite-based measurements of atmospheric ice can be performed with different types of sensors: active sensors such as radar and lidar, and passive sensors such as infrared imagery and passive microwave. In the following sections, relevant

Figure 1.5: Satellites featuring in this thesis that can be used for atmospheric ice mass retrievals. EarthCARE (the successor to CloudSat) carries, among others, a cloud profiling radar and a lidar, two active instruments. The Arctic Weather Satellite carries a passive radiometer with channels between 50 and 325 GHz. The MetOp-SG-B satellites carry the Ice Cloud Imager, a passive radiometer with channels between 183 and 664 GHz.

space-borne instruments types are introduced and how they have previously been used for atmospheric ice estimates. After that, two passive microwave and sub-millimetre instruments related to the work in this thesis are introduced.

1.3.1 Sensor types and ice property retrievals

Space-borne cloud profiling radars (CPRs) paired with lidar currently provide the most accurate measures for atmospheric ice. They offer high vertical resolution and sensitivity across a wide range of particle sizes through the synergy of lidar and active microwave measurements. These are *active* instruments, in the sense that they transmit pulses of energy and then record the response. Between 2006 and 2023 CloudSat (Stephens et al. 2002) was the first operational space-borne CPR, and on the same orbit the Cloud-Aerosol Lidar and infrared pathfinder satellite observations (CALIPSO) satellite performed lidar measurements. DARDAR (Cazenave et al. 2019) and 2C-ICE (Deng et al. 2015) are two data products that combine the radar and lidar data to produce ice property estimates. EarthCare (Illingworth et al. 2015; Wehr et al. 2023)

is the successor to the CloudSat (and CALIPSO duo): its playload features a CPR, a lidar, a visible and infrared imager, and a broadband radiometer. One ice property data product utilizing these instruments is ACM-CAP (Mason et al. 2023), currently in development.

The following sensor types are *passive*. Such sensors use the solar radiation or the thermal emission from Earth and atmosphere as the source. The radiation interacts with clouds and ice before reaching the instrument.

Wavelengths around $\lambda \approx 10\,\mu m$ are measured by thermal infrared (TIR) instruments, which are sensitive towards particles sizes at the lower end of particle sizes down to about $10\,\mu m$ and up to roughly $100\,\mu m$. Although such particles have a small mass compared to larger particles, they are more numerous and contribute significantly toward the FWC. However, for TIR radiation, extinction is strong, and from space, only the cloud-top will be visible. Infrared observations, in combination with visible measurements, have been employed to derive ice property data products from instruments such as MODIS (Platnick et al. 2003). However, such products have, since CloudSat's launch, been shown to underestimate the atmospheric ice mass (Duncan and Eriksson 2018). Machine learning-based methods of estimating ice mass from IR data, such as the Chalmers Cloud Ice climatology (CCIC; Amell et al. 2024) perform better in terms of average bias, perhaps owing to utilization of complex spatial relationships within the IR images in the retrieval method. For individual values, however, such estimates tend to show a varying bias compared to radar/lidar retrievals.

Passive microwave instruments measure at lower frequencies. The longer wavelengths provide sensitivity deeper into clouds and the atmosphere. By measuring at multiple frequencies, sensitivity to different altitudes can be achieved. The longer wavelengths make such instruments sensitive to larger particles and less sensitive to smaller ones.

Passive microwave sensors sensitive to sub-millimetre wavelengths have long been of interest due to their ability of sensing smaller particles (Gasiewski 1992; Evans and Stephens 1995). Limb-sounding measurements have provided additional insight (Wu et al. 2008; Eriksson et al. 2014) and airborne radiometer instruments have, through various measurements campaigns, provided data further demonstrating the retrieval capabilities for sub-millimetre frequencies (Brath et al. 2018), along with valuable in-situ data.

Sub-millimetre can offer accuracy comparable to radar-based retrievals whilst providing much larger spatial coverage (Pfreundschuh et al. 2020, 2022). Figure 1.6 illustrates the spatial coverage achieved by different sensor types over 45 min of observations. The active sensor has the smallest footprint, since a cloud profiling radar must point on one direction in order to focus the transmit and receive beam as far as possible. Passive microwave instruments achieve much wider coverage by passively measuring incoming radiance whilst scanning across the Earth's surface. Both instruments require low Earth orbit to keep antenna sizes and power consumption manageable. Passive infrared and visual

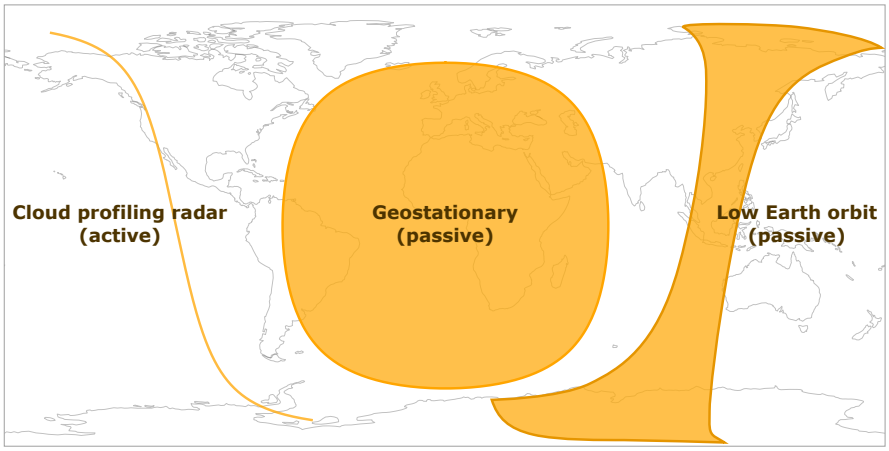

Figure 1.6: Spatial extent of different satellite orbit and sensor types for 45 minutes of observations. Cloud profiling radars have a footprint of about 1 km, a single low Earth orbit satellite can provide swaths of about 1000 km. One image from a geostationary satellite can provide a large field of view around the equator, but misses the poles.

imagery can provide the largest coverage, since they can operate at much higher orbits without practical complications. Aboard geostationary satellites, such instruments can observe the facing hemisphere, excluding polar regions, with short intervals. However, infrared measurements are not as directly sensitive to ice mass and related properties as microwave and sub-millimetre measurements. Sub-millimetre can provide more accurate estimates whilst still providing a larger spatial coverage than CPRs.

Up until 2024, there has been no satellite-based earth-facing sub-millimetre instrument providing regular and global measurements. This changed with the launch of the Arctic Weather Satellite.

1.3.2 The Arctic Weather Satellite

In August 2024, the Arctic Weather Satellite (AWS) was launched into a sun-synchronous orbit. It carries a radiometer sensitive to traditional passive microwave frequencies common to established weather satellites, as well as sub-millimetre frequencies, making it the first operational space-borne earth-facing sub-millimetre instrument. The instrument is an across-track scanner (scans perpendicular to the flight direction) and has 19 channels over four frequency bands: 50 GHz, 89 GHz, 183 GHz and 325 GHz. See Table 1.1a and Eriksson et al. (2025) for more information on the instrument.

The channels in the 50 GHz band are commonly used for sounding the temperature at different layers of the atmosphere. There is a *window* channel

(a) Arctic Weather Satellite

Channel	Frequency [GHz]	Bandwidth [GHz]
AWS11	50.300	0.18
AWS12	52.800	0.40
AWS13	53.246	0.30
AWS14	53.596	0.37
AWS15	54.400	0.40
AWS16	54.940	0.40
AWS17	55.500	0.33
AWS18	57.290	0.33
AWS21	89.000	4.00
AWS31	165.500	2.80
AWS32	176.311	2.00
AWS33	178.811	2.00
AWS34	180.311	1.00
AWS35	181.511	1.00
AWS36	182.311	0.50
AWS41	325.150 ± 1.2	2 × 0.80
AWS42	325.150 ± 2.4	2 × 1.20
AWS43	325.150 ± 4.1	2 × 1.80
AWS44	325.150 ± 6.6	2 × 2.80

(b) Ice Cloud Imager

Channel (Pol)	Frequency [GHz]	Bandwidth [GHz]
1 (V)	183.31 ± 7.0	2 × 2.00
2 (V)	183.31 ± 3.4	2 × 1.50
3 (V)	183.31 ± 2.0	2 × 1.50
4 (V,H)	243.20 ± 2.5	2 × 3.00
5 (V)	325.15 ± 9.5	2 × 3.00
6 (V)	325.15 ± 3.5	2 × 2.40
7 (V)	325.15 ± 1.5	2 × 1.60
8 (V)	448.00 ± 7.2	2 × 3.00
9 (V)	448.00 ± 3.0	2 × 2.00
10 (V)	448.00 ± 1.4	2 × 1.20
11 (V,H)	664.00 ± 4.2	2 × 5.00

Table 1.1: Channel centre frequencies and bandwidths for the Arctic Weather Satellite and the Ice Cloud Imager. AWS radiometer channel groups 1-3 (AWS11 to AWS36) are single sideband, whilst group 4 channels (AWS41 to AWS44) are double sideband. ICI radiometer channels are all double sideband and sensitive to vertical polarization (V), with some channels additionally measuring at horizontal polarization (H). AWS has varying polarization across its scan.

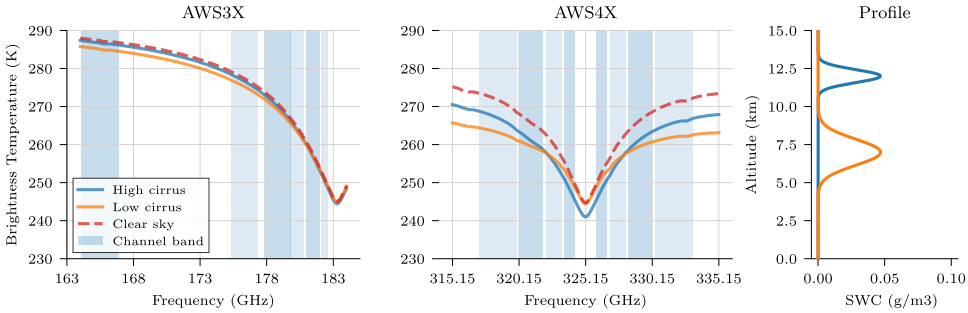

Figure 1.7: Simulated brightness temperature T_b radiance observed from space for two frequency ranges containing water vapour transition lines: 183 GHz and 325 GHz. The shaded regions indicate AWS channels, determined by their centre frequency and bandwidth. AWS4X channels are double sideband. Three cases are shown: clear-sky (no clouds), high-cirrus, and low-cirrus. The left-most panel shows the vertical profiles of snow water content (SWC) ($\mathrm{kg\,m^{-3}}$) for the cloudy cases. Figure adapted from Eriksson et al. (2025, CC BY 4.0).

at 89 GHz, chosen so that the atmosphere is as transparent as possible (for frequencies above 50 GHz), providing sensitivity down to the surface. The third group of channels are positioned with varying distance from the water vapour transition line at 183 GHz, providing sensitivity to the atmospheric humidity at different levels of the atmosphere. The sub-millimetre channels are similarly placed at varying distances to the water vapour transition line at 325 GHz. These channels provide sensitivity to water vapour, but also a heightened sensitivity towards ice hydrometeors.

The principles behind AWS's sensitivity to ice hydrometeors is illustrated in Figure 1.7. In the clear-sky case, radiance dips occur near the transition line frequencies. The dips extend from these lines due to pressure broadening of the absorption line, which provides information about the vertical extent of the atmospheric humidity.

The high cirrus case shows no discernible effect in the 183 GHz range, but shows an almost constant impact for 325 GHz relative to the clear-sky case. The low cirrus case shows a small effect for the 183 GHz range, but a stronger and varying effect across the 325 GHz range. Together, these cases demonstrate how the combination of 183 and 325 GHz channels can disentangle humidity from ice. Since clouds at different altitudes impact the 325 GHz channels differently, multiple channels can constrain the vertical extent of ice.

There were two main goals with AWS. First, to supply data for numerical weather prediction. Passive microwave measurements contain information on the atmospheric state regarding humidity and temperature. Weather centres have attributed much improved forecasting skill to such passive microwave measurements. A recent report shows that AWS contributes with significant

valuable data (Duncan et al. 2026). Second, to serve as a prototype for the EPS-Sterna constellation (Rivoire et al. 2024). The planned constellation consists of six copies of AWS, divided into three orbit planes (two satellites in each). The constellation will be replenished with two more batches of six satellites each. This will sustain a 13-year mission duration starting 2029.

1.3.3 The Ice Cloud Imager

The Ice Cloud Imager (ICI; Eriksson et al. 2020) is another radiometer that measures in the sub-millimetre. It is one of several instruments aboard EUMETSAT's MetOp Second Generation (MetOp-SG) B satellites, the first one due to launch later in 2026. With a total of three satellites, operations are expected to continue until 2048.

Like AWS, the instrument has channels near water vapour transition lines at 183.31 GHz and 325.15 GHz. It additionally measures at higher frequencies: 448.0 GHz (another water transition line), 243.2 GHz, and 664.0 GHz. See Table 1.1b for a complete channel list.

Beyond its higher frequencies and conical scan pattern, giving a constant surface incidence angle, ICI differentiates itself from AWS by measuring polarization. Most channels measure the vertical polarization component, whilst channel 4 and 11 measure both vertical and horizontal polarization. This extra information allows for constraining particle orientations.

1.4 Research context

The work presented in this thesis directly builds upon previous work. This section briefly presents previous key contributions.

Early sub-millimetre research As mentioned in Section 1.3.1, passive microwave sensors sensitive to sub-millimetre wavelengths have been of research interest. Simulations from the 1990s and onward demonstrated their sensitivity to ice (Gasiewski 1992; Evans and Stephens 1995; Evans et al. 2002). Later their ability to resolve vertical distribution of ice (Evans et al. 2012) was demonstrated. Different measurements campaigns from airborne instruments to limb-sounding satellites have further validated their capabilities (Wu et al. 2008; Eriksson et al. 2014; Brath et al. 2018). In an effort to further utilize sub-millimetre, multiple satellite missions have been proposed (Miao et al. 2002; Buehler et al. 2012), paving the way for the Ice Cloud Imager.

Radiative transfer simulation framework Extensive radiative transfer simulations have been performed during this work. For these simulations, the "Atmospheric Radiative Transfer simulator" (ARTS; Buehler et al. 2025) has been used: a simulation framework for simulating satellite or ground-based instrument observations of the atmosphere. With this framework, scenes are set up with surface emission, atmospheric absorption from gases and

scattering particles. With such scenes and a model of an instrument, satellite T_b measurements can be simulated.

Database of single-scattering properties For accurate simulations of clouds, scattering ice hydrometeor need to be properly represented. As mentioned in section 1.2.4, single-scattering properties (SSPs) are needed to describe how scattering particles in a medium will affect the measured radiance. Previous work created geometric representations of particle shapes and aggregates in order to simulate how electromagnetic radiation interacts with them. This resulted in a database of SSPs for multiple particle shapes, sizes, polarizations, and frequencies extending to the sub-millimetre range (Eriksson et al. 2018).

Quantile regression neural networks In remote sensing, *inversion* is the process of going from measurement value to estimated physical quantity. There are multiple inversion methods, and ideally they should handle the "ill-posed" nature of many inversion problems, meaning that there are multiple valid physical quantities for a given measurement, an inherent uncertainty in these problems that must be described in any estimate. Bayesian methods have previously been employed for this purpose since they allow for a natural way to model distributions of estimated values. However, such methods become impractical when the relationship between measurement and physical quantity becomes complex and non-linear. Machine learning methods excel at learning and handling non-linear relationships and are able to provide very plausible estimates. However, there has been little emphasis on such methods to describe uncertainty.

Quantile regression neural networks (QRNNs) are a machine learning approach for estimating quantiles (the distribution) of the physical quantities given measurement values, in addition to point estimates. Previous work (Pfreundschuh et al. 2018) evaluated such a method for remote sensing inversions and demonstrated that it is a suitable alternative to Bayesian approaches.

Preparations for the Ice Cloud Imager The Ice Cloud Imager and the preparations for it have been ongoing for many years. Studies, simulations, and test flight campaigns have all provided valuable insights, methods and data for developing ice property retrievals. For example, the database of single-scattering properties was partly motivated by the ICI instrument, airborne instruments like ISMAR (Fox et al. 2017) provided early data for a sub-millimetre instrument similar to ICI, and multiple methods for ice property retrievals have been worked on. In this thesis, the methodology behind the simulations and retrievals builds on the ice property retrieval work developed for ICI in May et al. (2024).

Starting point The European Space Agency signed the contract for the Arctic Weather Satellite in 2021. The satellite launched in August 2024, three years later. The work presented in this thesis began a few months before that launch and is aimed towards evaluating these new measurements and utilizing them for ice property estimates.

Chapter 2

Summary of appended papers

2.1 Paper 1

In "The Arctic Weather Satellite, introducing a new wavelength range for ice hydrometeor retrievals", we present a dataset of ice mass property retrievals from AWS. The dataset provides FWP, Z_m (the mean mass-weighted altitude of ice) and D_m (the mean mass-weighted d_{veq}). These regular and global ice mass estimates are the first of its kind to utilize sub-millimetre channels, providing improved sensitivity to ice hydrometeors among passive observations.

Since no prior global sub-millimetre observations exists, simulating the new instrument was necessary. This resulted in a large set of synthetic instrument measurements with known physical scene parameters. The resulting large set of measurement and parameter pairs are then used to implement a retrieval method for AWS.

Comparing simulated AWS measurements against real AWS observation shows that simulations overall achieve a close match with observations and manage to the distribution of measurements from a wide range of atmospheric scenarios. With simulated measurements and corresponding parameters, the utility of the instrument channels for extracting ice property information can be synthetically evaluated. This evaluation shows that AWS instrument channels provide good sensitivity to retrieve average ice mass, ice particle sizes and their vertical distribution. Synthetic comparisons also suggest substantially improved accuracy over other passive datasets.

Statistical comparisons of retrievals performed on actual AWS observations with an external radar/lidar-derived ice property datasets show matching local and zonal means. This confirms that retrieved ice property estimates from real observations are reasonable.

These ice property estimates are continuously processed and openly provided as a data product: `http://clouds-and-precip.group/datasets/chip-aws`.

2.2 Paper 2

In "A first global view of sub-millimetre radiances from the Arctic Weather Satellite" the novelty of the AWS instrument is presented and explored, and the ability for radiative transfer models to recreate the new sub-millimetre observations is evaluated. Such models are used by numerical weather prediction (NWP) and a proper recreation is necessary for the information to be properly utilized by weather centres.

The new 325 GHz channels, combined with others, provides enhanced sensitivity and information on ice. A degree-of-freedom analysis and correlations between FWP and cloud signals demonstrate that these channels add information and sensitivity to thinner clouds.

From an NWP perspective, two radiative transfer models (RTTOV and ARTS) are compared against real AWS measurements to assess whether this band's behaviour is sufficiently represented. ARTS, a scientific research model, and RTTOV, the operational radiative transfer model used by ECMWF for data assimilation, successfully model the new band. This suggests that ECMWF and other weather centres using RTTOV can already assimilate some of this new information, yet improvements remain possible.

Bibliography

Amell, A., S. Pfreundschuh and P. Eriksson (2024). "The Chalmers Cloud Ice Climatology: retrieval implementation and validation". In: *Atmos. Meas. Tech.* 17.14, pp. 4337–4368. DOI: 10.5194/amt-17-4337-2024 (cit. on p. 14).

Bojinski, S., M. Verstraete, T. C. Peterson, C. Richter, A. Simmons and M. Zemp (2014). "The Concept of Essential Climate Variables in Support of Climate Research, Applications, and Policy". In: *Bulletin of the American Meteorological Society* 95.9, pp. 1431–1443. DOI: 10.1175/BAMS-D-13-00047.1 (cit. on p. 3).

Brath, M., S. Fox, P. Eriksson, R. C. Harlow, M. Burgdorf and S. A. Buehler (2018). "Retrieval of an ice water path over the ocean from ISMAR and MARSS millimeter and submillimeter brightness temperatures". In: *Atmospheric Measurement Techniques* 11.1, pp. 611–632. DOI: 10.5194/amt-11-611-2018 (cit. on pp. 14, 18).

Buehler, S. A., E. Defer, F. Evans et al. (2012). "Observing ice clouds in the submillimeter spectral range: the CloudIce mission proposal for ESA's Earth Explorer 8". In: *Atmos. Meas. Tech.* 5.7, pp. 1529–1549. DOI: 10.5194/amt-5-1529-2012 (cit. on p. 18).

Buehler, S. A., R. Larsson, O. Lemke, S. Pfreundschuh, M. Brath, I. Adams, S. Fox, F. E. Roemer, P. Czarnecki and P. Eriksson (2025). "The atmospheric radiative transfer simulator ARTS, version 2.6 — Deep python integration". In: *J. Quant. Spectrosc. Radiat. Transfer* 341, p. 109443. ISSN: 0022-4073. DOI: 10.1016/j.jqsrt.2025.109443 (cit. on p. 18).

Cazenave, Q., M. Ceccaldi, J. Delanoë, J. Pelon, S. Groß and A. Heymsfield (2019). "Evolution of DARDAR-CLOUD ice cloud retrievals: new parameters and impacts on the retrieved microphysical properties". In: *Atmospheric Measurement Techniques* 12.5, pp. 2819–2835. DOI: 10.5194/amt-12-2819-2019 (cit. on p. 13).

Deng, M., G. G. Mace, Z. Wang and E. Berry (2015). "CloudSat 2C-ICE product update with a new Ze parameterization in lidar-only region". In: *Journal of Geophysical Research: Atmospheres* 120.23, pp. 12, 198–12, 208. DOI: 10.1002/2015JD023600 (cit. on p. 13).

Duncan, D. I., N. Bormann, M. Crepulja, M. Dahoui, A. J. Geer, C. Accadia, S. Di Michele, T. J. Hewison and V. Kangas (2026). "Arctic Weather Satellite Assessment and Assimilation at ECMWF". In: *EGUsphere* 2026, pp. 1–29. DOI: 10.5194/egusphere-2026-712 (cit. on p. 18).

Duncan, D. I. and P. Eriksson (2018). "An update on global atmospheric ice estimates from satellite observations and reanalyses". In: *Atmos. Chem. Phys.* 18.15, pp. 11205–11219. DOI: 10.5194/acp-18-11205-2018 (cit. on p. 14).

Eriksson, P., R. Ekelund, J. Mendrok, M. Brath, O. Lemke and S. A. Buehler (2018). "A general database of hydrometeor single scattering properties at microwave and sub-millimetre wavelengths". In: *Earth Syst. Sci. Data* 10.3, pp. 1301–1326. DOI: 10.5194/essd-10-1301-2018 (cit. on pp. 9, 19).

Eriksson, P., A. Emrich, K. Kempe et al. (2025). "The Arctic Weather Satellite radiometer". In: *Atmos. Meas. Tech.* 18.18, pp. 4709–4729. DOI: 10.5194/amt-18-4709-2025 (cit. on pp. 15, 17).

Eriksson, P., B. Rydberg, V. Mattioli, A. Thoss, C. Accadia, U. Klein and S. A. Buehler (2020). "Towards an operational Ice Cloud Imager (ICI) retrieval product". In: *Atmos. Meas. Tech.* 13.1, pp. 53–71. DOI: 10.5194/amt-13-53-2020 (cit. on p. 18).

Eriksson, P., B. Rydberg, H. Sagawa, M. S. Johnston and Y. Kasai (2014). "Overview and sample applications of SMILES and Odin-SMR retrievals of upper tropospheric humidity and cloud ice mass". In: *Atmos. Chem. Phys.* 14.23, pp. 12613–12629. DOI: 10.5194/acp-14-12613-2014 (cit. on pp. 14, 18).

Evans, K. F. and G. L. Stephens (1995). "Microwave radiative transfer through clouds composed of realistically shaped ice crystals. Part II. Remote sensing of ice clouds". In: *J. Atmos. Sci.* 52.11, pp. 2058–2072 (cit. on pp. 14, 18).

Evans, K. F., J. R. Wang, D. O'C Starr, G. Heymsfield, L. Li, L. Tian, R. P. Lawson, A. J. Heymsfield and A. Bansemer (2012). "Ice hydrometeor profile retrieval algorithm for high-frequency microwave radiometers: application to the CoSSIR instrument during TC4". In: *Atmospheric Measurement Techniques* 5.9, pp. 2277–2306. DOI: 10.5194/amt-5-2277-2012 (cit. on p. 18).

Evans, K. F., S. J. Walter, A. J. Heymsfield and G. M. McFarquhar (2002). "Submillimeter-Wave Cloud Ice Radiometer: Simulations of retrieval algorithm performance". In: *Journal of Geophysical Research: Atmospheres* 107.D3, AAC 2-1-AAC 2–21. DOI: https://doi.org/10.1029/2001JD000709 (cit. on p. 18).

Field, P. R. and A. J. Heymsfield (2015). "Importance of snow to global precipitation". In: *Geophysical Research Letters* 42.21, pp. 9512–9520. DOI: 10.1002/2015GL065497 (cit. on p. 4).

Fox, S., C. Lee, B. Moyna et al. (2017). "ISMAR: an airborne submillimetre radiometer". In: *Atmospheric Measurement Techniques* 10.2, pp. 477–490. DOI: 10.5194/amt-10-477-2017 (cit. on p. 19).

Gasiewski, A. (1992). "Numerical sensitivity analysis of passive EHF and SMMW channels to tropospheric water vapor, clouds, and precipitation". In: *IEEE T. Geosci. Remote* 30.5, pp. 859–870. DOI: 10.1109/36.175320 (cit. on pp. 14, 18).

Illingworth, A. J., H. W. Barker, A. Beljaars et al. (2015). "The EarthCARE Satellite: The Next Step Forward in Global Measurements of Clouds, Aerosols, Precipitation, and Radiation". In: *Bulletin of the American Meteorological*

Society 96.8, pp. 1311–1332. DOI: 10.1175/BAMS-D-12-00227.1 (cit. on p. 13).

Intergovernmental Panel on Climate Change (IPCC) (2023). "Technical Summary". In: *Climate Change 2021 – The Physical Science Basis: Working Group I Contribution to the Sixth Assessment Report of the Intergovernmental Panel on Climate Change*. Cambridge University Press, pp. 35–144. DOI: 10.1017/9781009157896.002 (cit. on pp. 3, 5).

Lohmann, U., F. Lüönd and F. Mahrt (2016). *An Introduction to Clouds: From the Microscale to Climate*. Cambridge University Press. DOI: 10.1017/CBO9781139087513 (cit. on pp. 4, 5).

Marshall, J. S. and W. M. K. Palmer (1948). "The Distribution of Raindrops with Size". In: *Journal of Atmospheric Sciences* 5.4, pp. 165–166 (cit. on p. 10).

Mason, S. L., R. J. Hogan, A. Bozzo and N. L. Pounder (2023). "A unified synergistic retrieval of clouds, aerosols, and precipitation from EarthCARE: the ACM-CAP product". In: *Atmospheric Measurement Techniques* 16.13, pp. 3459–3486. DOI: 10.5194/amt-16-3459-2023 (cit. on p. 14).

May, E., B. Rydberg, I. Kaur, V. Mattioli, H. H. and P. Eriksson (2024). "The Ice Cloud Imager: retrieval of frozen water column properties". In: *Atmos. Meas. Tech.* 17.19. DOI: 10.5194/amt-17-5957-2024 (cit. on p. 19).

Miao, J., T. Rose, K. Kunzi and P. Zimmermann (2002). "A Future Millimeter/Sub–Millimeter Radiometer for Satellite Observation of Ice Clouds". In: *Int. J. Inf. Millim. Waves* 23.8, pp. 1159–1170 (cit. on p. 18).

Pfreundschuh, S., P. Eriksson, S. A. Buehler, M. Brath, D. Duncan, R. Larsson and R. Ekelund (2020). "Synergistic radar and radiometer retrievals of ice hydrometeors". In: *Atmospheric Measurement Techniques* 13.8, pp. 4219–4245. DOI: 10.5194/amt-13-4219-2020 (cit. on p. 14).

Pfreundschuh, S., P. Eriksson, D. Duncan, B. Rydberg, N. Håkansson and A. Thoss (2018). "A neural network approach to estimating a posteriori distributions of Bayesian retrieval problems". In: *Atmospheric Measurement Techniques* 11.8, pp. 4627–4643. DOI: 10.5194/amt-11-4627-2018 (cit. on p. 19).

Pfreundschuh, S., S. Fox, P. Eriksson, D. Duncan, S. A. Buehler, M. Brath, R. Cotton and F. Ewald (2022). "Synergistic radar and sub-millimeter radiometer retrievals of ice hydrometeors in mid-latitude frontal cloud systems". In: *Atmospheric Measurement Techniques* 15.3, pp. 677–699. DOI: 10.5194/amt-15-677-2022 (cit. on p. 14).

Platnick, S., M. King, S. Ackerman, W. Menzel, B. Baum, J. Riedi and R. Frey (2003). "The MODIS cloud products: algorithms and examples from Terra". In: *IEEE Transactions on Geoscience and Remote Sensing* 41.2, pp. 459–473. DOI: 10.1109/TGRS.2002.808301 (cit. on p. 14).

Rivoire, L., R. Marty, T. Carrel-Billiard, P. Chambon, N. Fourrié, O. Audouin, M. Martet, C. Birman, C. Accadia and J. Ackermann (2024). "A global observing-system simulation experiment for the EPS–Sterna microwave constellation". In: *Q. J. R. Meteorol. Soc.* 150(762), pp. 2991–3012. DOI: 10.1002/qj.4747 (cit. on p. 18).

Sharkov, E. A. (2003). *Passive microwave remote sensing of the earth*. en. 2003rd ed. Geophysical Sciences. Berlin, Germany: Springer (cit. on p. 5).

Stephens, G. L., D. G. Vane, R. J. Boain, G. G. Mace, K. Sassen, Z. Wang, A. J. Illingworth, E. J. O'connor, W. B. Rossow, S. L. Durden et al. (2002). "The CloudSat mission and the A-Train: A new dimension of space-based observations of clouds and precipitation". In: *Bull. Amer. Met. Soc.* 83.12, pp. 1771–1790 (cit. on p. 13).

Ulaby, F. and D. Long (2014). *Microwave radar and radiometric remote sensing*. University of Michigan Press (cit. on p. 5).

Wallace, J. M. and P. V. Hobbs (2006). Second Edition. San Diego: Academic Press, pp. 471–483. ISBN: 978-0-12-732951-2. DOI: 10.1016/B978-0-12-732951-2.50018-1 (cit. on pp. 5, 8).

Wehr, T., T. Kubota, G. Tzeremes, K. Wallace, H. Nakatsuka, Y. Ohno, R. Koopman, S. Rusli, M. Kikuchi, M. Eisinger et al. (2023). "The EarthCARE mission–science and system overview". In: *Atmos. Meas. Tech.* 16.15, pp. 3581–3608 (cit. on p. 13).

World Meteorological Organization (2016). *The Global Observing System for Climate: Implementation Needs*. WMO. URL: https://library.wmo.int/idurl/4/55469 (cit. on p. 3).

Wu, D. L., J. H. Jiang, W. G. Read, R. T. Austin, C. P. Davis, A. Lambert, G. L. Stephens, D. G. Vane and J. W. Waters (2008). "Validation of the Aura MLS cloud ice water content measurements". In: *Journal of Geophysical Research: Atmospheres* 113.D15 (cit. on pp. 14, 18).